*Article*

# Chemo-Mechanical Coupling Measurement of LiMn$_2$O$_4$ Composite Electrode during Electrochemical Cycling

Huijie Yu [1], Jiangtao Li [1], Hainan Jiang [1], Wei Li [2], Guorui Li [2] and Dawei Li [1,*]

[1] School of Mechanical Engineering, University of Shanghai for Science and Technology, Shanghai 200093, China
[2] State Key Laboratory of Space Power-Sources Technology, Shanghai Institute of Space Power-Source, Shanghai 200245, China
* Correspondence: lidawei@usst.edu.cn

**Abstract:** Real-time monitoring of the mechanical behavior of cathode materials during the electrochemical cycle can help obtain an in-depth understanding of the working mechanism of lithium-ion batteries. The LiMn$_2$O$_4$ composite electrode is employed as the working electrode in this artificial cell, which is conceived and produced along with a chemo-mechanical coupling measurement system. The multi-layer beam composite electrode made of LiMn$_2$O$_4$ is monitored in real time using a CCD camera to track its curvature deformation. Experiments show that the curvature of the LiMn$_2$O$_4$ electrode decreases with the extraction of lithium ions and increases during the lithiation process. In the meantime, a theoretical framework was developed to examine the connection between curvature change and mechanical characteristics. Thus, the elastic modulus, strain, and stress of the LiMn$_2$O$_4$ composite electrode were extracted by combining the bending deformation and theoretical model. The results show that the elastic modulus of the LiMn$_2$O$_4$ composite electrode decreases from 59.61 MPa to 12.01 MPa with the extraction of lithium ions during the third cycle. Meanwhile, the stress decreases from 0.46 MPa to 0.001 MPa, and the strain reduces from 0.43 to 0. Its changes reverse during the lithiation process. Those findings could have made a further understanding of the mechanical properties in lithium-ion batteries.

**Keywords:** LiMn$_2$O$_4$ composite electrode; elastic modulus; strain; stress; lithium-ion batteries

## 1. Introduction

Lithium batteries are essential for the rapid development of clean energy worldwide due to its high energy density and long cycle life [1]. Currently, it has been widely used for the storage of intermittent and sustainable energy, such as wind power and hydropower [2]. Mechanical degradation of electrodes is widely recognized as a key contributor to the decline in the performance of lithium-ion batteries over time. Therefore, research on the mechanical degradation of electrodes has attracted much attention [3,4].

Usually, lattice changes appear in the electrode materials during the delithiation/lithiation process, which causes volume change and stress evolution of the batteries [5–8]. Several studies have found that the cycle performance and mechanical properties of cathode materials are closely related. In situ experiments on LiFePO$_4$/FePO$_4$ electrodes have shown that there is a mismatch between the valence change of Fe ions and the transformation from LiFePO$_4$ to FePO$_4$ during the delithiation process. The structural changes cause the heterogeneous strain of LiFePO$_4$ by adjusting the volume [9]. In the experiment, the lower cycle performance of NCM811 is caused by significant cracks and irreversible structural degradation [10]. The volume change, which is caused by delithiation and lithiation in the ceramic oxide electrode (usually cathode) systems, is typically in the range of 0 to 10% [11,12]. However, due to the brittleness of the cathode material, even small volume changes can have a great effect on the cycling performance of the battery electrodes [13,14].

Dokko, K. et al. studied the morphological changes of $LiNiO_2$ particles in the electrochemical cycle by an in situ observation technology. It was found that the structural instability was due to the crystal stress caused by charge and discharge process [15]. Haifeng Wang et al. used transmission electron microscopy (TEM) to analyze the micro-structure damage of $LiCoO_2$ electrodes during electrochemical cycling, including lattice strain, extended defects, and micro-fracture [16]. Miller, D. J. et al. found that the physical separation and isolation of $Li(Ni_{0.8}Co_{0.15}Al_{0.05})O_2$ particles may lead to the performance degradation of lithium-ion batteries [17]. The $LiMn_2O_4$ cathode has several advantages over other cathode materials, including its low cost, non-toxicity, high working voltage, and excellent safety performance [18,19]. In the $LiMn_2O_4$ battery electrode, the tetragonal phase structure has better stability than the cubic one [20]. The cubic phase structure of $LiMn_2O_4$ electrodes is changeable during the electrochemical cycles, and even obvious volume expansion will occur [21]. Those factors could result in the low cyclic performance of $LiMn_2O_4$ electrodes, which is a constraint on the extensive application of the $LiMn_2O_4$ cathode system [22,23]. Thus, the cycle performance degradation-inducing factors of $LiMn_2O_4$ electrodes has attracted widespread attention [24,25]. Hao et al. noted the micro-fracture in the LMO particle cycle in the experiment and believed that the capacity decay was related to mechanical failure [26]. Therefore, it is necessary to develop new theoretical and experimental platforms to explore the mechanical degradation of the $LiMn_2O_4$ composite electrode.

The In situ experimental platform can better explore the evolution of the mechanical properties of battery electrodes. To better explore the mechanical behavior of electrode materials during charge and discharge processes, various in situ experimental platforms have been developed such as nanoindentation, atomic force microscopy (AFM), multiple-beam optical stress sensing (MOSS), and so on [27–29]. The combination of various in situ experimental platforms and microscopic characterizations can obtain the mechanical properties and microscopic morphology of the electrode in multiple directions and analyze the degradation of the electrode's active layer [30,31]. Amani et al. obtained the elastic modulus and hardness data of the $LiMn_2O_4$ electrode in the electrochemical cycle by a selective statistical nanoindentation experiment. The mechanical degradation of the $LiMn_2O_4$ electrodes can greatly affect the cycling performance of the batteries [27]. Yang et al. applied bimodal atomic force microscopy to investigate the surface morphology of $LiMn_2O_4$ electrodes and the variation in elastic modulus. Additionally, the deterioration of mechanical properties and the relationship between surface morphology and the elastic modulus variation were analyzed [28]. Jay Sheth et al. explored the stress evolution throughout the charge–discharge cycle of LMO electrodes during the real-time measurements using the MOSS experimental platform and the Stoney equation [29]. Previous studies have found that the capacity decay of the $LiMn_2O_4$ electrode is closely related to mechanical failure. Most of the empirical literature focused on the mechanical evolution of the $LiMn_2O_4$ films. In this work, the commercially used electrode with a porous structure was used as the experimental electrode. During the electrochemical cycling, the mechanical properties of the electrode material change due to structural changes during the delithiation/lithiation process. The mechanical degradation of the $LiMn_2O_4$ composite electrode has been explored.

In this work, the chemo-mechanical response of the $LiMn_2O_4$ composite electrode was explored. In the experiment, the macroscopic curvature change of the double-layer beam electrode was measured by the CCD optical in situ test system. At the same time, according to the volume deformation of the $LiMn_2O_4$ electrode in the process of delithiation/lithiation, a mechanical model was constructed to explore the development of the mechanical degradation of the $LiMn_2O_4$ composite electrode during the electrochemical cycle. The mechanical degradation of the $LiMn_2O_4$ composite electrode in the electrochemical cycle is closely related to changes in the elastic modulus, strain, and stress. The study mainly explores the mechanical behavior of $LiMn_2O_4$ composite electrodes during electrochemical cycling and obtains a basic mechanical parameter. Through chemo-mechanical testing and mechanical parameter analysis, it is revealed that the mechanical degradation of the $LiMn_2O_4$ composite electrode will cause the deterioration of the electrochemical performance.

## 2. Experiment and Method

### 2.1. Electrode Preparation

$LiMn_2O_4$ active particles (size:1.9~9.9 μm, MTI), conductive carbon black (Super P, MTI), and polyvinylidene fluoride (PVDF, MTI) were mixed at a mass ratio of 90:5:5. Here, PVDF was used as the binder and helped enhance the physical connection between the component, while carbon black was used to improve the conductivity. Firstly, $LiMn_2O_4$ active particles and a conductive agent powder were mixed and stirred in a horizontal planetary ball mill (MSK-SFM-13S, MTI). PVDF was completely dissolved in N-methyl-2-pyrrolidone (NMP, 99.9%, MTI) solvent and stirred by water bath heating. Then, the PVDF/NMP solution was added to the $LiMn_2O_4$ active particles/conductive agent mixture for wet mixing and then placed in the planetary ball mill for stirring to obtain a uniformly dispersed electrode slurry. Then, the electrode slurry was coated using the auto thick film coater (MSK-AFA-II-VC, MTI). The coating rate is 60 cm/min, and the thickness of the current collector aluminum foil is 16 μm. After the coating was completed, the electrode was dried in a vacuum drying at 90 °C for 12 h. The thickness of the active layer of the $LiMn_2O_4$ composite electrode was about 64 μm. The mass loading and porosity of the experimental electrode are 14.18 mg/cm$^2$ and 29.7%, respectively. Figure 1 shows the microscopic morphology of the surface of the original $LiMn_2O_4$ oxide composite electrode. It can be seen from Figure 1a that the electrode surface is in a very dense active particle, and there is no obvious crack. Figure 1b is the local enlarged graph of Figure 1a, and it can be seen that there are dense gaps and holes between the active particles. This porous structure improves the utilization of the active material area. It allows the double conduction of Li$^+$ and electrons which also alleviates the structural strain and volume change of the active layer [32].
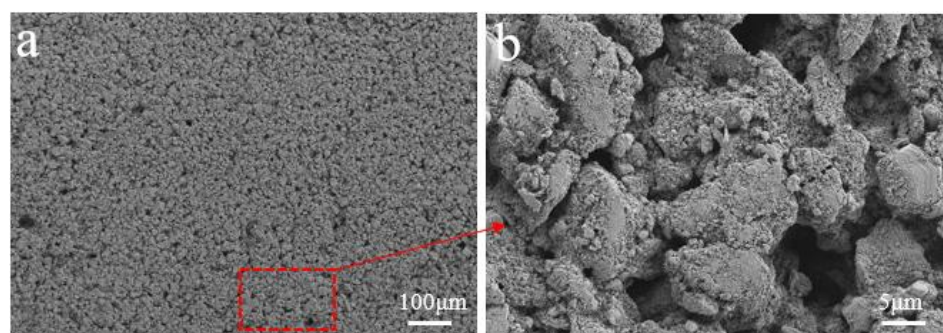


**Figure 1.** Surface microstructure of a pristine $LiMn_2O_4$ composite electrode (**a**) and (**b**) at different magnifications.

### 2.2. Chemo-Mechanical Measurement System

Figure 2 shows the schematic diagram of the chemical–mechanical measurement system in this work. The chemical–mechanical test system is mainly composed of artificial cells, an image acquisition system, and a data analysis system. Among them, Computer1 is responsible for collecting the experimental electrode bending deformation pictures taken by the CCD camera in real-time and linking the data processing system to collect the curvature data in different pictures. Computer2 is mainly used for electrochemical testing of artificial cells.

The artificial cell mainly consists of a lower positioning seat, a battery compartment, a sealing gasket, a sealing cover, a top positioning cover, and attached bolts, as shown in Figure 1. In this work, the $LiMn_2O_4$ composite electrode was designed as the working electrode and the commercial graphite electrode (theoretical capacity of 330 mAh/g) was treated as the anode in the artificial cell. The sealing cover is a highly transparent quartz material which allows the CCD video camera (JAI, CM200GE) to monitor the deformation in real-time. A microporous polypropylene film (thickness of 21 μm, Celgard) is used to separate the graphite electrodes from the $LiMn_2O_4$ composite electrode. Then, enough elec-

trolyte was added into the cell to fully immerse the electrode. The battery was assembled and tested in the electrochemical glove box (O$_2$ < 0.01 ppm, H$_2$O < 0.01 ppm, MIKROUNA) filled with argon.
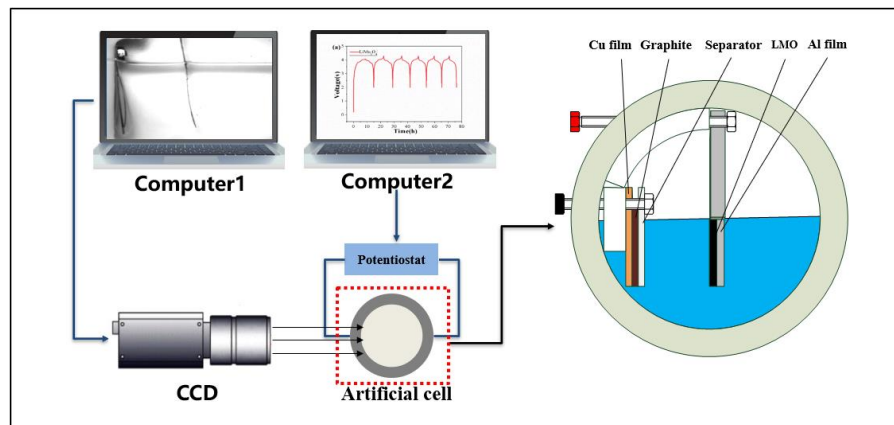


**Figure 2.** Schematics of the chemo-mechanical measurement system and the artificial cell (cross-section).

### 2.3. The Electrochemical Test

After the assembly of the cell, it rested for 12 h which makes sure that the LiMn$_2$O$_4$ composite electrode is fully wetted by the electrolyte. Then, the artificial cell was cycled by the battery test system (NEWARE) at room temperature. The theoretical specific capacity of the LiMn$_2$O$_4$ electrode was 148 mAh/g and the charging/discharging rate was set as C/10. Accordingly, the current density was calculated to be 188.9 μA/cm$^2$. The voltage was set in the range of 2 to 4.3 V.

The artificial cell underwent a 9 h cycle followed by a 3 min open-circuit potential relaxation. During the charge–discharge cycle, the experimental data acquisition system was applied to capture the process of bending deformation to LiMn$_2$O$_4$ composite electrode in real-time. The data acquisition system automatically captures the images of experimental electrode deformation at a rate of every two minutes.

### 2.4. Mechanical Mode of LiMn$_2$O$_4$ Composite Electrode

A mathematical model was established to explore the bending deformation mechanism of the LiMn$_2$O$_4$ composite electrode. As shown in Figure 3a, the active layer is attached to the current collector to form a cantilever beam model. Herein, the thicknesses of the active layer and current collector are indicated by the letters h$_1$ and h$_C$, respectively. During the delithiation/lithiation process, the extraction/insertion of the lithium ions in the LiMn$_2$O$_4$ particles could cause contraction/expansion of the active layer.
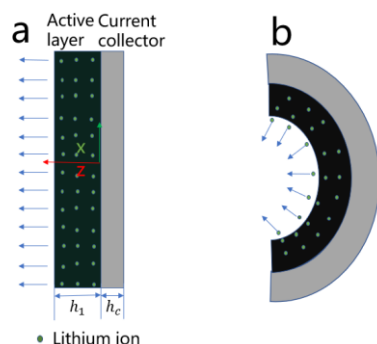


**Figure 3.** The structure of the electrode, wherein an active plate is combined with the current collector ((**a**) initial state and (**b**) deformation state).

The electrode bends to generate a larger (smaller) curvature as a result of the current collector's constraint, as depicted in Figure 3b. The thickness was aligned along the $z$-axis, with the interface located in the $x$–$y$ plane. Here, the in-plane normal strain can be depicted as [33]: $\varepsilon = \varepsilon_0 + \kappa z$, where $\varepsilon_0$ is considered as contraction strain at $z = 0$, which indicates the contraction of the electrode, and $\kappa$ is the curvature. The active layer of the LiMn$_2$O$_4$ electrode and the current collector are assumed to be tightly combined during the electrochemical cycling. Therefore, they have the same curvature during the deformation process.

Typically, composite electrodes have a complex structure consisting of active particles, binders, conductive agents, and internal pores. In this work, the LiMn$_2$O$_4$ composite electrodes are assumed to have macroscopic elasticity and uniformity. Furthermore, the LiMn$_2$O$_4$ electrode was cycled at a considerably lower charge rate (equal to 0.1 $C$-rate); thus, the lithium ions concentration was assumed to be a constant. The following is a representation of the constitutive equation for the active layer and current collector [33]:

$$\begin{cases} \sigma_1 = E_1(\varepsilon_0 + \kappa z) - \frac{1}{3}E_1\Omega c \\ \sigma_c = E_c(\varepsilon_0 + \kappa z) \end{cases} \tag{1}$$

Here, $E_1$ represents the elastic modulus of the LiMn$_2$O$_4$ electrode layer, and $\Omega$ represents the partial molar volume and was defined as a function of concentration. Concentration-related items $-1/3\,E_1\Omega c$ represents the diffusion-induced stress of the active layer. The stress and toque balances require:

$$\int_{-h_c}^{h_1} \sigma_x dz = 0 \int_{-h_c}^{h_1} \sigma_x z dz = 0 \tag{2}$$

By substituting Equation (1) into Equation (2), the elastic modulus and contraction strain are obtained as follows.

$$E_1 = \frac{2\kappa h_1 \gamma_h{}^4 E_c}{-(4\kappa h_1\gamma_h + 6\kappa h_1\gamma_h{}^2 + 4\kappa h_1\gamma_h{}^3 - 2\Omega c\gamma_h - 2\Omega c\gamma_h{}^2) + \sqrt{(4\kappa h_1\gamma_h + 6\kappa h_1\gamma_h{}^2 + 4\kappa h_1\gamma_h{}^3 - 2\Omega c\gamma_h - 2\Omega c\gamma_h{}^2)^2 - 4\kappa^2 h_1\gamma_h{}^4 h_1}} \tag{3}$$

$$\varepsilon_0 = \frac{\kappa\left(\frac{1}{2}E_1 h_1^2 - \frac{1}{2}E_c h_c^2\right) - \frac{1}{3}E_1\Omega_c h_1}{(E_c h_c + E_1 h_1)} \tag{4}$$

In Equation (3), $\gamma_h$ is used to represent the thickness ratio and $\gamma_h = h_c/h_1$. By substituting Equation (3) and Equation (4) into Equation (1) and Equation (2), the analytical formula is obtained for the relationship between stress, strain, and curvature. The curvature deformation of the LiMn$_2$O$_4$ composite electrode during electrochemical cycling was detected using a CCD camera. According to the above equation, the elastic modulus, strain, and stress of the LiMn$_2$O$_4$ composite electrode were measured in real-time during cycling.

## 3. Results and Discussion

The voltage and curvature change with the insertion and extraction of the lithium ions, as shown in Figure 4. It shows the voltage change diagram of the six cycles of LiMn$_2$O$_4$. It can be found that the voltage platform is low and unstable in the first cycle, and the voltage platform is stable at 2–4.3 V in the second cycle. When lithium ions are continuously removed from the LiMn$_2$O$_4$ composite electrode, the active layer of the composite electrode will shrink, meanwhile, the current collector restricts its shrinkage. With the extraction of lithium ions, the curvature of the electrode gradually decreases, and the insertion process is reversed. As shown in Figure 4b, it can be seen that the curvature change of the LiMn$_2$O$_4$ composite electrode in the first cycle is quite different from other cycles. This is mainly due to the formation of a solid electrolyte interface phase (SEI) during the initial cycle, which leads to the large consumption of lithium ions.
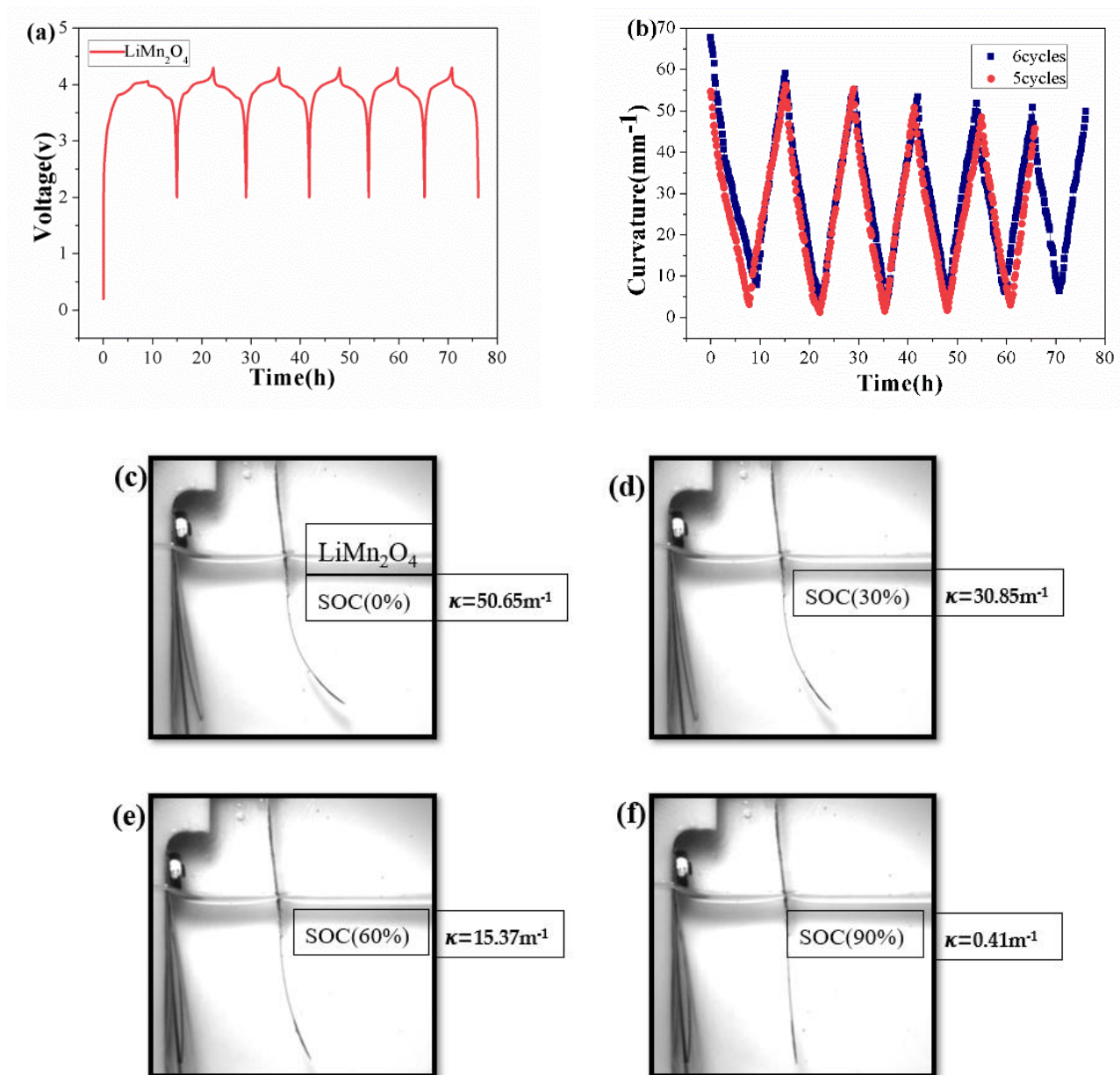
**Figure 4.** (**a**) Voltage and (**b**) curvature evolution of the $LiMn_2O_4$ composite electrode during the electrochemical cycles. The captured images of the bilayer beam electrode in the initial state (**c**) and working state (**d**–**f**).

As shown in Figure 4c, the $LiMn_2O_4$ composite electrode is in the initial state of the third cycle. Figure 4d shows the electrode began to shrink and deform with the extraction of lithium ions. Figure 4e shows that the experimental electrode has a more obvious shrinkage deformation in the SOC60%. As shown in Figure 4f, at the end of the lithium removal stage, the shrinkage deformation of the experimental electrode stops. It can be found that the extraction of lithium ions from the active layer will cause an obvious bending deformation of the $LiMn_2O_4$ composite electrode. During the insertion process, the volume deformation of the $LiMn_2O_4$ composite electrode increases, which is opposite to the delithiation process.

During the delithiation process, the lithium ions are continuously extracted from the active layer. The mismatch could cause the bending deformation of the bilayer electrode. With more lithium ions removed from the active material, the curvature decreases, which results in a round shape of the entire electrode. The deformation with the extraction of lithium ions is opposite to the insertion process. Figure 5a shows the charging curvature

change of the LiMn$_2$O$_4$ composite electrode for six cycles in the experiment. During the cycling process, the curvature changes gradually stabilized from the second cycle. There is a significant difference between the curvature evolution of the first cycle and other cycles. The formation of unstable SEI on LiMn$_2$O$_4$ particles cannot effectively protect the electrode surface from side reactions with proton electrolytes, which affects the lithium intercalation/deintercalation of the LiMn$_2$O$_4$ composite electrode [34]. Due to the inconsistency in the electrochemical performance of the first cycle LiMn$_2$O$_4$ battery, there is a considerable difference in the curvature change to other cycles. Through Figure 5a, we can conclude that the curvature change of the experimental electrode tends to be stable during the third cycle. Therefore, the curvature data in the third cycle are used to analyze the chemo-mechanical response of the LiMn$_2$O$_4$ composite electrode. Subsequently, the mechanical properties of the third cycle charging and discharging process were characterized according to Equation (1), Equation (3), and Equation (4). As shown in Figure 5b, the curvature coincidence degree of the LiMn$_2$O$_4$ electrode is higher in the third cycle. Experiment (2) is a control experiment, which also proves the stable and reversible bending deformation of the LiMn$_2$O$_4$ electrode in the third cycle.
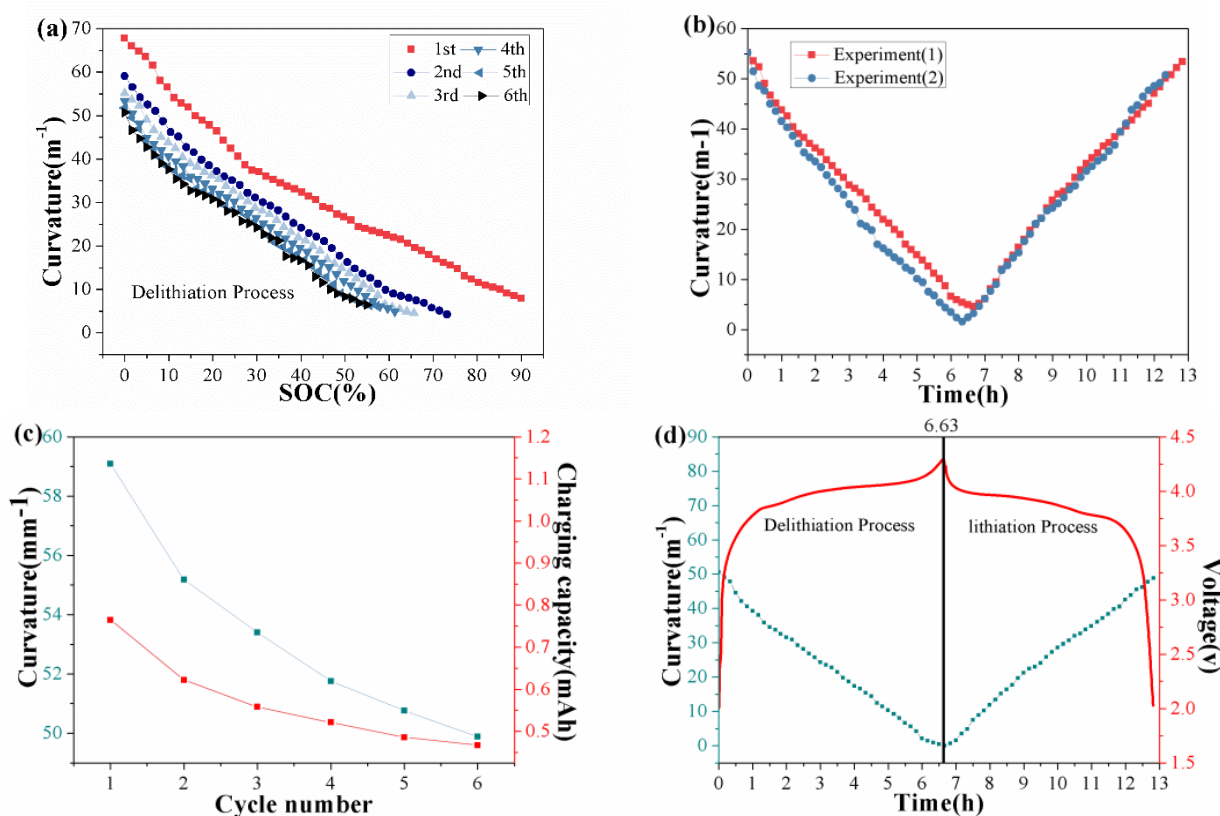


**Figure 5.** (**a**) Curvature changes of the LiMn$_2$O$_4$ composite electrode in the delithiation process, (**b**) curvature comparison during the third cycle in the different experiments, (**c**) curvature and charging capacity evolution at the end of each cycle, and (**d**) voltage and curvature evolution in the third cycle.

As shown in Figure 5c, the curvature of the LiMn$_2$O$_4$ electrode in the six experimental cycles gradually decreases. The curvature was 59.09 m$^{-1}$ after the first cycle of lithium insertion and decreases to 49.88 m$^{-1}$ in the sixth cycle, while the charging capacity of the LiMn$_2$O$_4$ battery also decreases from 0.76 mAh in the first cycle to 0.47 mAh in the sixth cycle. As shown in Figure 5d, the voltage and curvature change of the LiMn$_2$O$_4$ composite electrode in the third cycle are characterized. With the extraction of lithium ions, the curvature begins to decrease from 50.65 m$^{-1}$ to 0.41 m$^{-1}$. During the insertion process, the curvature of the experimental electrode begins to increase gradually and stops

growing at 12.8 h, and the curvature was 48.87 m$^{-1}$. It can be seen that at the end of the third cycle, the curvature is less than at the beginning of the cycle. It indicates that the composite electrode has slight mechanical degradation during the electrochemical cycle.

Depending on Equation (3), the correlation between the change in curvature, thickness ratio, and elastic modulus can be obtained. Among them, $\Omega$ represents the partial molar volume and expresses the volume change when the active layer is completely lithiated. For LiMn$_2$O$_4$, the volumetric strain (of unit cell volume) is about 7.5% [3]. The current collector is an aluminum foil with the elastic modulus is 72 GPa. In this work, the elastic modulus is defined as the average of the entire LiMn$_2$O$_4$ composite electrode, including the effects of porosity, structural change, and fracture. As shown in Figure 6a, the elastic modulus of the LiMn$_2$O$_4$ composite electrode declines sharply from 59.61 MPa to 12.01 MPa during the third cycle with the extraction of lithium ions. During the insertion process, the average elastic modulus of the active layer of the LiMn$_2$O$_4$ composite electrode rises from 12.01 MPa to 56.75 MPa. The results reveal that the elastic modulus of the LiMn$_2$O$_4$ composite electrode suddenly decreased after SOC50%. The dissolution of manganese and the onset of J-T distortion at higher potentials due to dynamic non-equilibrium conditions during the cycling process will cause the capacity attenuation of LiMn$_2$O$_4$ in the 4 V region [35]. After SOC50%, it is just the interval of the voltage in the 4 V region, and the growth rate of the voltage in this interval also begins to increase. It can be concluded that the extraction of lithium ions in this interval is unstable, resulting in a sudden decrease in elastic modulus, which is also true during the insertion process.
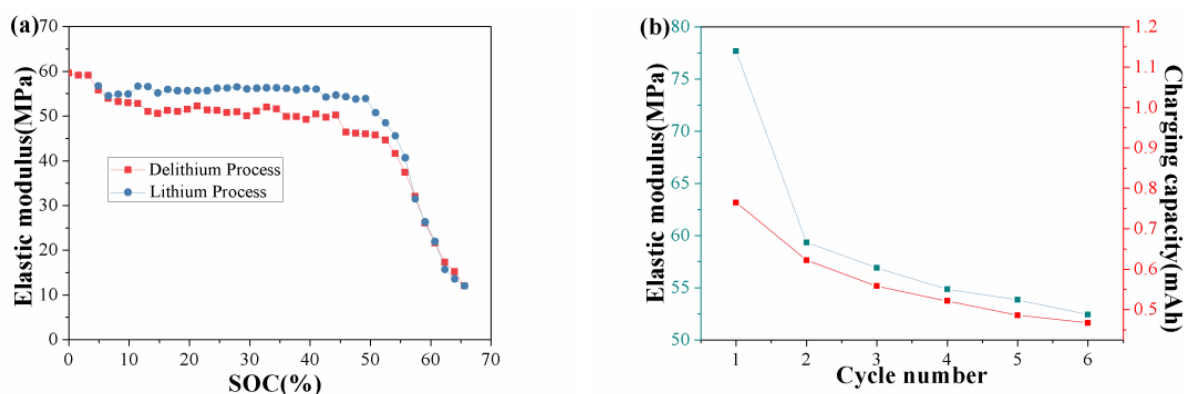


**Figure 6.** Elastic modulus evolution of LiMn$_2$O$_4$ composite electrodes with time in the (**a**) delithiation/lithiation process of the 3rd cycle and (**b**) the end of the lithiation process in each cycle.

Figure 6b shows the elastic modulus and charging capacity change of the LiMn$_2$O$_4$ composite electrode at the end of each cycle. The elastic modulus at the end of the first cycle is 77.66 MPa and reduces to 52.43 MPa at the end of the sixth cycle. The charging capacity of the LiMn$_2$O$_4$ battery also decreases from 0.76 mAh to 0.47 mAh during the electrochemical cycle. The data indicated that the Mn ions were the charge–transfer centers [20]. In the delithiation/lithiation process, the LiMn$_2$O$_4$ composite electrode is continuously subjected to the dissolution of Mn$^{3+}$ as well as the loading and unloading of stress, which results in a continuous decline in the average elastic modulus of the active layer of LiMn$_2$O$_4$ composite electrode [36]. Researchers have found that irreversible structural changes of the electrode in the first cycle are common in lithium-ion batteries. Lithium-rich manganese layered oxide $_X$Li$_2$MnO$_3$·$_{(1-X)}$LiMO$_2$ (M = Ni, Co) loses oxygen during the first delithiation process, resulting in a stable structural configuration at the end of the first decomposition, supporting reversible delithiation/lithiation during subsequent cycles [37]. It can be found that in the electrochemical experiment, compared with other adjacent cycles, the elastic modulus and charging capacity decreased significantly from the first cycle to the second cycle. It indicates that the LiMn$_2$O$_4$ composite electrode forms a relatively stable structure from the second cycle.

Substituting the calculation results of Equation (3) and curvature data into Equation (4), the contraction strain can be obtained. Similarly, the stress can be obtained by substituting the results of Equation (3), Equation (4), and curvature data into Equation (1). During the electrochemical cycle, the reversible evolution of the 'electrode strain' of $LiMn_2O_4$ measured by the bending beam method (BBM) [38]. Figure 7a shows that the strain of the $LiMn_2O_4$ composite electrode in the third experimental cycle has a certain reversibility during the cycle. During the delithiation process, the active layer exhibits shrinkage and deformation due to the migration of lithium ions, resulting in a gradual decrease in the strain. The current collector prevents the volume expansion of the active material during the lithiation process, resulting in a linear increase in the absolute value of the strain under the insertion process. With the extraction of lithium ions, the strain reduces from 0.43 to 0. During the insertion process, the strain of the $LiMn_2O_4$ composite electrode showed an increasing trend during further lithiation, and the strain increases linearly to 0.39.
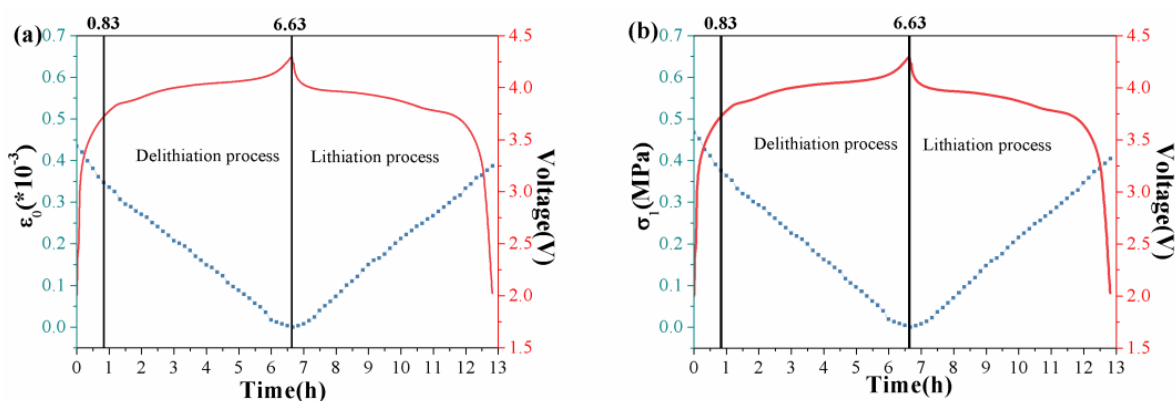


**Figure 7.** (**a**) Contraction strain–voltage and (**b**) stress–voltage evolution during the 3rd cycle of the $LiMn_2O_4$ composite electrode at 0.1 C.

As shown in Figure 7b, with the extraction of lithium ions, the stress reduces to 0.001 MPa. During the insertion process, with the continuous process of lithium intercalation, the stress increases linearly at 12.8 h to 0.40 MPa. It has different orders of magnitude from the stress evolution results of the $LiMn_2O_4$ electrode reported by MOSS [29]. The experimental electrode in the MOSS system is a thin film electrode, and the magnitude of stress is small in this paper is a composite electrode with a microscopic porous structure. The lattice parameters of lithium manganate will change greatly in a low voltage range, which makes it difficult to maintain the integrity of the crystal structure during the cycle. It has a better performance in a higher voltage range [39]. It shows that the strain and stress unloading rates are relatively fast in the $LiMn_2O_4$ composite electrode from 0 to 0.83 h in the lower voltage range. From 0.83 h to 6.63 h, the strain and stress unloading rates are relatively slow at higher voltage platforms.

During the electrochemical cycle, the electrode undergoes obvious bending deformation. The surface morphology of the electrode in the third electrochemical cycle was examined by scanning electron microscopy (SEM) at different magnifications. It can be seen from Figure 8 that the active layer of the $LiMn_2O_4$ composite electrode did not produce obvious cracks significantly during the third cycle. It shows that the active layer of the $LiMn_2O_4$ composite electrode has good integrity during the cycle. As shown in Figure 8c, the characterization results at a large magnification show that the active particles of the $LiMn_2O_4$ composite electrode present a rich porous structure. It shows that more pores grow on the surface of the active layer at the end of the delithiation process. As shown in Figure 8d, due to the occurrence of expansion strain, the pores between the active particles are reduced during the lithiation process. It can be concluded that more pores appear during the delithiation process due to structural strain and lithium ions extraction. During the insertion process, the pores decrease, and the active layer maintains marvelous integrity

in the electrochemical cycle. It is shown that the structure of the LiMn$_2$O$_4$ composite electrode has a relatively stable reversible change during the electrochemical cycle.
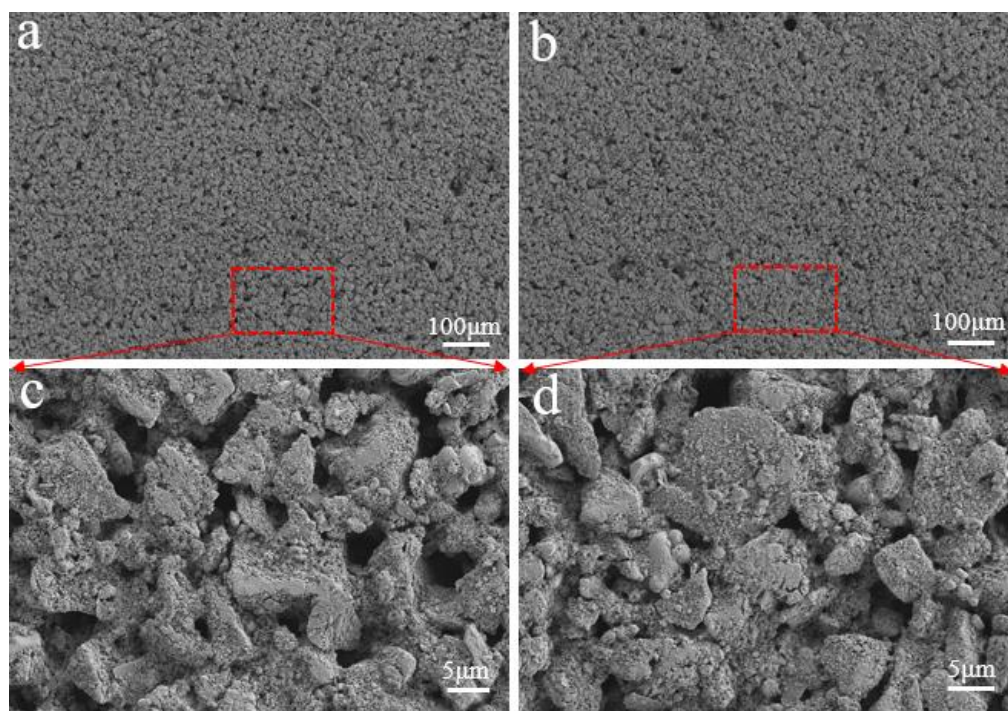


**Figure 8.** Surface microstructure of LiMn$_2$O$_4$ composite electrode during the third cycle (**a,c**) fully delithiated (**b,d**) and fully lithiated at different magnifications.

## 4. Conclusions

In this work, a chemo-mechanical measurement system was developed to test the elastic modulus, strain, and stress evolution of commercial cathode materials during the electrochemical cycles. The curvature of the LiMn$_2$O$_4$ composite electrode decreases linearly during the delithiation process and reverses during the lithiation process. Based on the curvature change of the experimental electrode, the model of the mechanical properties of the composite electrode was established. In summary, the change of the elastic modulus during the third cycle and the evolution of the elastic modulus at the end of each cycle were obtained. During the electrochemical cycles, the elastic modulus decreases from 77.66 MPa at the onset of the first cycle to 52.43 MPa at the end of the sixth cycle. In the third cycling, it decreases from 59.61 MPa to 12.01 MPa with the extraction of lithium ions and increases from 12.01 MPa to 56.75 MPa during the insertion process. The strain decreases from 0.43 to 0, and the stress reduces to 0.001 MPa. It can be found that the strain and stress of the LiMn$_2$O$_4$ composite electrode decrease with the decrease in lithium-ion concentration. Within the insertion process, the strain increases from 0 to 0.39, and stress increases linearly to 0.40 MPa. It shows that the strain and stress generated by the electrochemical reaction increase with further lithiation. In addition, it can be found that in the delithiation process, the unloading rate of strain and stress changes faster at lower potentials. The chemo-mechanical coupling test system in this paper can obtain basic mechanical properties in a single measurement. It can analyze the mechanical behavior of the electrode at different voltage platforms. These mechanical performance data help to develop battery models. In addition, the chemo-mechanical experimental method can also describe the components' influence on the mechanical properties of the composite electrode, which provides a direction for developing the electrode with stable cycle performance.

**Data Availability Statement:** Experiment data were under further consideration and will be supplied later.

**Conflicts of Interest:** The authors declare no conflict of interest.

# References

1. Xie, J.; Liang, Z.; Lu, Y.C. Molecular crowding electrolytes for high-voltage aqueous batteries. *Nat. Mater.* **2020**, *19*, 1006–1011. [CrossRef] [PubMed]
2. Jia, Z.; Qin, P.; Li, Z.; Wei, Z.; Jin, K.; Jiang, L.; Wang, Q. Analysis of gas release during the process of thermal runaway of lithium-ion batteries with three different cathode materials. *J. Energy Storage* **2022**, *50*, 104302. [CrossRef]
3. Mukhopadhyay, A.; Sheldon, B.W. Deformation and stress in electrode materials for Li-ion batteries. *Prog. Mater. Sci.* **2014**, *63*, 58–116. [CrossRef]
4. Chen, Z.; Danilov, D.L.; Eichel, R.A.; Notten, P.H.L. Porous Electrode Modeling and its Applications to Li-Ion Batteries. *Adv. Energy Mater.* **2022**, *12*, 2201506. [CrossRef]
5. Li, D.; Wang, Y.; Lu, B.; Zhang, J. Real-time measurements of electro-mechanical coupled deformation and mechanical properties of commercial graphite electrodes. *Carbon* **2020**, *169*, 258–263. [CrossRef]
6. Martens, I.; Vostrov, N.; Mirolo, M.; Colalongo, M.; Kúš, P.; Richard, M.-I.; Wang, L.; Zhu, X.; Schülli, T.U.; Drnec, J. Revisiting Phase Transformation Mechanisms in $LiNi_{0.5}Mn_{1.5}O_4$ High Voltage Cathodes with Operando Microdiffraction. *ACS Mater. Lett.* **2022**, *4*, 2528–2536. [CrossRef]
7. Alikin, D.; Slautin, B.; Kholkin, A. Revealing Lithiation Kinetics and Battery Degradation Pathway in LiMn2O4-Based Commercial Cathodes via Electrochemical Strain Microscopy. *Batteries* **2022**, *8*, 220. [CrossRef]
8. Fuller, E.J.; Ashby, D.S.; Polop, C.; Salagre, E.; Bhargava, B.; Song, Y.; Vasco, E.; Sugar, J.D.; Albertus, P.; Mentes, T.O.; et al. Imaging Phase Segregation in Nanoscale Li(x)CoO(2) Single Particles. *ACS Nano* **2022**, *16*, 16363–16371. [CrossRef]
9. Chen, H.; Kim, S.; Huang, H.-Y.S. Exploration of the dislocation-electrochemistry relation in $LiFePO_4$ cathode materials. *Acta Mater.* **2022**, *237*, 118158. [CrossRef]
10. Cao, B.; Li, Y.; Zhang, M.; Cheng, N.; Shen, M.; Hu, B.; Li, J.; Li, Z.; Xu, S.; Zhao, W.; et al. Sb@Ni6 superstructure units stabilize Li-rich layered cathode in the wide voltage window. *J. Power Sources* **2022**, *551*, 232148. [CrossRef]
11. Kim, M.; Kang, S.; Gyu Park, H.; Park, K.; Min, K. Maximizing the energy density and stability of Ni-rich layered cathode materials with multivalent dopants via machine learning. *Chem. Eng. J.* **2023**, *452*, 139254. [CrossRef]
12. Kim, S.; Na, S.; Kim, J.; Jun, T.H.; Oh, M.H.; Min, K.; Park, K. Multifunctional surface modification with Co-free spinel structure on Ni-rich cathode material for improved electrochemical performance. *J. Alloys Compd.* **2022**, *918*, 165454. [CrossRef]
13. Zhu, H.; Wang, Z.; Chen, L.; Hu, Y.; Jiang, H.; Li, C. Strain Engineering of Ni-Rich Cathode Enables Exceptional Cyclability in Pouch-Type Full Cells. *Adv. Mater.* **2022**, *35*, 2209357. [CrossRef] [PubMed]
14. Santos, D.A.; Rezaei, S.; Zhang, D.; Luo, Y.; Lin, B.; Balakrishna, A.R.; Xu, B.-X.; Banerjee, S. Chemistry–mechanics–geometry coupling in positive electrode materials: A scale-bridging perspective for mitigating degradation in lithium-ion batteries through materials design. *Chem. Sci.* **2023**, *14*, 458–484. [CrossRef] [PubMed]
15. Dokko, K.; Nishizawa, M.; Horikoshi, S.; Itoh, T.; Mohamedi, M.; Uchida, I. In situ observation of $LiNiO_2$ single-particle fracture during Li-ion extraction and insertion. *Electrochem. Solid State Lett.* **2000**, *3*, 125–127. [CrossRef]
16. Wang, H.F.; Jang, Y.I.; Huang, B.Y.; Sadoway, D.R.; Chiang, Y.T. TEM study of electrochemical cycling-induced damage and disorder in $LiCoO_2$ cathodes for rechargeable lithium batteries. *J. Electrochem. Soc.* **1999**, *146*, 473–480. [CrossRef]
17. Miller, D.J.; Proff, C.; Wen, J.G.; Abraham, D.P.; Bareño, J. Observation of Microstructural Evolution in Li Battery Cathode Oxide Particles by In Situ Electron Microscopy. *Adv. Energy Mater.* **2013**, *3*, 1098–1103. [CrossRef]
18. Xu, G.; Liu, Z.; Zhang, C.; Cui, G.; Chen, L. Strategies for improving the cyclability and thermo-stability of $LiMn_2O_4$-based batteries at elevated temperatures. *J. Mater. Chem. A* **2015**, *3*, 4092–4123. [CrossRef]
19. Fu, Y.; Jiang, H.; Hu, Y.; Dai, Y.; Zhang, L.; Li, C. Synergistic Enhancement Effect of Al Doping and Highly Active Facets of $LiMn_2O_4$ Cathode Materials for Lithium-Ion Batteries. *Ind. Eng. Chem. Res.* **2015**, *54*, 3800–3805. [CrossRef]
20. Abdollahifar, M.; Huang, S.-S.; Lin, Y.-H.; Sheu, H.-S.; Lee, J.-F.; Lu, M.-L.; Liao, Y.-F.; Wu, N.-L. Tetragonal $LiMn_2O_4$ as dual-functional pseudocapacitor-battery electrode in aqueous Li-ion electrolytes. *J. Power Sources* **2019**, *412*, 545–551. [CrossRef]
21. Tang, M.; Yuan, A.; Zhao, H.; Xu, J. High-performance $LiMn_2O_4$ with enwrapped segmented carbon nanotubes as cathode material for energy storage. *J. Power Sources* **2013**, *235*, 5–13. [CrossRef]

22. Asakura, D.; Nanba, Y.; Makinose, Y.; Matsuda, H.; Hosono, E. Investigation of the relationship between the cycle performance and the electronic structure in LiAl(x)Mn(2−x)O(4) (x = 0 and 0.2) using soft X-ray spectroscopy. *Phys. Chem. Chem. Phys.* **2017**, *19*, 16507–16511. [CrossRef] [PubMed]

23. Xiang, J.; Zhang, P.; Lv, S.; Ma, Y.; Zhao, Q.; Sui, Y.; Ye, Y.; Qin, C. Spinel LiMn$_2$O$_4$ nanoparticles fabricated by the flexible soft template/Pichini method as cathode materials for aqueous lithium-ion capacitors with high energy and power density. *RSC Adv.* **2021**, *11*, 14891–14898. [CrossRef] [PubMed]

24. Liu, D.; Su, Z.; Wang, L. Pyrometallurgically regenerated LiMn$_2$O$_4$ cathode scrap material and its electrochemical properties. *Ceram. Int.* **2021**, *47*, 42–47. [CrossRef]

25. Chen, Z.-L.; Gu, Y.-J.; Huo, Y.-L.; Ma, X.-Y.; Wu, F.-Z. Enhanced electrochemical performance of manganese-based metal organic frameworks-derived spinel LiMn$_2$O$_4$ cathode materials by improving the Mn3+ content and oxygen vacancies. *J. Alloys Compd.* **2022**, *917*, 165485. [CrossRef]

26. Hao, X.; Lin, X.; Lu, W.; Bartlett, B.M. Oxygen vacancies lead to loss of domain order, particle fracture, and rapid capacity fade in lithium manganospinel LiMn$_2$O$_4$ batteries. *ACS Appl. Mater. Interfaces* **2014**, *6*, 10849–10857. [CrossRef]

27. Amanieu, H.-Y.; Rosato, D.; Sebastiani, M.; Massimi, F.; Lupascu, D.C. Mechanical property measurements of heterogeneous materials by selective nanoindentation: Application to LiMn$_2$O$_4$ cathode. *Mater. Sci. Eng. A* **2014**, *593*, 92–102. [CrossRef]

28. Yang, P.; Bi, Z.; Shang, Y.; Chen, K.; Liang, Y.; Li, X.; Shang, G. Bimodal AFM-Based Nanocharacterization of Cycling-Induced Topographic and Mechanical Evolutions of LiMn$_2$O$_4$ Cathode Films. *Langmuir* **2021**, *37*, 6406–6413. [CrossRef]

29. Sheth, J.; Karan, N.K.; Abraham, D.P.; Nguyen, C.C.; Lucht, B.L.; Sheldon, B.W.; Guduru, P.R. In Situ Stress Evolution in Li1+xMn$_2$O$_4$Thin Films during Electrochemical Cycling in Li-Ion Cells. *J. Electrochem. Soc.* **2016**, *163*, A2524–A2530. [CrossRef]

30. Kang, D.; Warburton, R.E.; Mane, A.U.; Greeley, J.; Elam, J.W. Modification of LiMn$_2$O$_4$ surfaces by controlling the Acid–Base surface chemistry of atomic layer deposition. *Appl. Surf. Sci.* **2022**, *599*. [CrossRef]

31. Meng, X.; Bi, Z.; Wang, X.; Shang, G. A novel design for the combination of electrochemical atomic force microscopy and Raman spectroscopy in reflection mode for in situ study of battery materials. *Rev. Sci. Instrum.* **2022**, *93*, 073707. [CrossRef] [PubMed]

32. Ali, K.; Raza, H.A.; Malik, M.I.; Ibn Shamsah, S.; Amna, R.; Sarfraz, A. To Study the Effect of LiMn$_2$O$_4$, Nanofibers of LiMn$_2$O$_4$, and Graphene/Polyaniline/Carbon Nanotube as Electrode Materials in the Fuel Cell. *J. New Mater. Electrochem. Syst.* **2020**, *23*, 1–6. [CrossRef]

33. Zhang, J.; Lu, B.; Song, Y.; Ji, X. Diffusion induced stress in layered Li-ion battery electrode plates. *J. Power Sources* **2012**, *209*, 220–227. [CrossRef]

34. Phan, Q.T.N.; Kawamura, J.; Kurihara, K. Effect of vinylene carbonate on SEI formation on LiMn$_2$O$_4$ in carbonate-based electrolytes. *Phys. Chem. Chem. Phys.* **2022**, *24*, 25611–25619. [CrossRef] [PubMed]

35. Jang, D.H.; Shin, Y.J.; Oh, S.M. Dissolution of spinel oxides and capacity losses in 4 V Li/LixMn$_2$O$_4$ cells. *J. Electrochem. Soc.* **1996**, *143*, 2204–2211. [CrossRef]

36. De Taeye, L.L.; Vereecken, P.M. Chemo-mechanical effect of chlorine modified TiO$_2$ coatings on LMO. *J. Mater. Chem. A* **2022**, *10*, 24398–24409. [CrossRef]

37. Armstrong, A.R.; Holzapfel, M.; Novak, P.; Johnson, C.S.; Kang, S.-H.; Thackeray, M.M.; Bruce, P.G. Demonstrating oxygen loss and associated structural reorganization in the lithium battery cathode Li[Ni$_{0.2}$Li$_{0.2}$Mn$_{0.6}$O]$_2$. *J. Am. Chem. Soc.* **2006**, *128*, 8694–8698. [CrossRef]

38. Chung, K.Y.; Shu, D.; Kim, K.B. Determination of the potential range responsible for the replacement of surface film on LiMn$_2$O$_4$. *Electrochim. Acta* **2004**, *49*, 887–898. [CrossRef]

39. Thackeray, M.M. Spinel Electrodes for Lithium Batteries. *J. Am. Ceram. Soc.* **2004**, *82*, 3347–3354. [CrossRef]